A Visualization of the Global Dynamic Tropopause

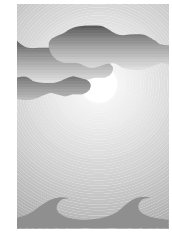

John W. Nielsen-Gammon
Department of Atmospheric Sciences, Texas A&M University, College Station, Texas

ABSTRACT

A 20-yr loop of the global tropopause, defined in terms of potential vorticity (PV), is constructed using the NCEP–NCAR reanalysis dataset. This method of visualizing observed upper-tropospheric dynamics is useful for studying a wide range of phenomena. Examples are given of the structure of jet streams and planetary-scale tropopause folds, the propagation of a high-amplitude Rossby wave packet partway around a hemisphere, several subtropical wave breaking events, the similarities between exceptional cases of rapid cyclogenesis, favorable regions for cross-equatorial propagation of Rossby waves, the annual cycle of the tropical tropopause, the structure of the Tibetan anticyclone and equatorial easterly jet associated with the Asian monsoon, the meridional structure of the upper branch of the Hadley cell, the interaction of a hurricane and midlatitude trough to form the "Perfect Storm," and the upper-tropospheric PV changes associated with El Niño and La Niña.

Plumes of anticyclonic potential vorticity are frequently seen to be pulled from the subtropical reservoir and roll up into large anticyclones. These previously undescribed plumes may be particularly relevant to jet streak dynamics and stratosphere–troposphere exchange.

1. Introduction

Recent reanalysis projects, such as those by the National Centers for Environmental Prediction and National Center for Atmospheric Research (NCEP–NCAR; Kalnay et al. 1996), the European Centre for Medium-Range Weather Forecasts (ECMWF; Gibson et al. 1997), and the National Aeronautical and Space Administration (Schubert et al. 1993), have generated global analyses of meteorological variables spanning several decades. The use of fixed data assimilation schemes minimizes artificial discontinuities in the datasets, although the quality of the analyses will vary according to the availability and quality of conventional and satellite data and the underlying numerical model (e.g., Newman et al. 2000; Randel et al. 2000; Santer et al. 1999). The visualization of such a continuous dataset would allow individuals to develop a conceptual understanding of the behavior of the atmosphere on a variety of space and time scales, by making use of the visual processing abilities of the human brain (McIntyre 1988).

Any such visualization may only depict a small number of basic or derived parameters. It is critical that the visualized fields convey the maximum amount of information on the state of the atmosphere, while simultaneously providing easily assimilated information on the evolution of the atmosphere. Potential vorticity (PV) possesses most of these desirable characteristics. PV (on an isentropic surface) is conserved following the two-dimensional isentropic flow, so its evolution is visually intuitive and provides direct information on the advecting winds. PV is also related to the large-scale height or pressure fields through a balance condition, so the instantaneous distribution of PV implies a specific configuration of heights, temperatures, and winds: the invertibility principle (Hoskins et al. 1985; Raymond 1992; Davis et al. 1996; McIntyre and Norton 2000).

PV is also compact, in the sense that the largest PV variations in the upper troposphere and lower stratosphere are concentrated along the tropopause, so upper-level synoptic-scale features (troughs, jets, etc.)

Corresponding author address: John W. Nielsen-Gammon, Dept. of Atmospheric Sciences, Texas A&M University, 3150 TAMU, College Station, TX 77843-3150.
E-mail: n-g@tamu.edu
In final form 26 January 2001.

usually can be related directly to variations in the location of the tropopause PV gradient along isentropic surfaces (Hoskins et al. 1985). Indeed, the concentrated PV gradient is often used to identify the tropopause itself (e.g., Hoerling et al. 1991 and references therein), and we shall adopt that convention here. However, multiple isentropic surfaces intersect the tropopause, so several isentropic maps would be needed to provide a global specification of the location of this dynamic tropopause.

This problem is neatly circumvented if one overlays the location of the tropopause at several evenly spaced isentropic levels onto a single map. Such a map, called a tropopause map, is identical to a map of potential temperature on a constant PV surface within the tropopause, as long as the height of the tropopause is singly valued. A tropopause map retains the advantages of isentropic PV maps: conservation (potential temperature on a PV surface is conserved following adiabatic and frictionless flow) and invertibility [directly, as in Thorpe (1986) or Juckes (1994), or indirectly, by specifying a three-dimensional PV distribution consistent with the tropopause location]. Furthermore, the compactness of PV is exploited by condensing the three-dimensional PV distribution onto a two-dimensional map. Tropopause maps were introduced by Hoskins and Berrisford (1988) and have since been applied to a wide range of phenomena. See Morgan and Nielsen-Gammon (1998) for an extensive discussion of methods for constructing tropopause maps, applications of tropopause maps to diagnosing synoptic-scale weather systems, and a list of published papers that make use of tropopause maps.

Tropopause maps form the basis of the 20-yr global visualization described in this article. The visualization consequently emphasizes processes taking place in the upper troposphere. In section 2, the technique for constructing the global tropopause maps is presented and the image format and layout are described. In section 3, examples of phenomena and processes visible in the tropopause loop, some well known and others poorly understood, are discussed. Finally, section 4 contains information on acquiring the full loop or viewing images.

2. Technical details

a. Data

The source of data is the NCEP–NCAR reanalysis (Kalnay et al. 1996). For the loop, 6-h reanalysis data were acquired for the period January 1978 through April 1998. The incorporation of satellite temperature retrievals into the global assimilation data began in November 1978, although some satellite data were assimilated in the Southern Hemisphere throughout 1977 and 1978 (Kalnay et al. 1996; Santer et al. 1999). This loop starts in January 1978 rather than November 1978 so as to begin at a new year and to include significant eastern United States weather events during the first two months of 1978.

Comparisons of parallel assimilations with and without satellite data indicate large differences in temperature and wind in the tropical upper troposphere and in the distribution and strength of eddies, with forecasts initialized with assimilated satellite data performing better than forecasts without, even when scored against no-satellite analyses (Mo et al. 1995). Upper-tropospheric reanalyses prior to November 1978 rely heavily on model forecasts over the oceans and over the Southern Hemisphere, while reanalyses for November 1978 and beyond rely heavily on retrieved satellite data in those places. The data discontinuity produces an artificial analysis discontinuity in fields such as lower-stratospheric temperature (Santer et al. 1999).

Reanalysis data were obtained in the form of spherical harmonic coefficients at T62 resolution on the 28 native sigma surfaces. The data were then converted to a corresponding Gaussian grid. Next, potential vorticity was computed on the sigma surfaces, and the PV and other parameters were then linearly interpolated (with respect to sigma) to isentropic surface from 260 to 370-K at 5 K increments. In order to exclude high values of PV in the lower troposphere, the PV was flagged as missing wherever isentropic surfaces were below 650 mb.

b. Tropopause maps

The tropopause maps were constructed using the fill overlay method (Morgan and Nielsen-Gammon 1998). Beginning at 370 K, areas with stratospheric values of PV ($|\mathrm{PV}| > 1.5$ PVU) are shaded a particular color. The same is done for the next lowest level, with a slightly different color. Since the portion of the 365-K surface within the stratosphere is typically smaller than the portion of the 370-K surface within the stratosphere, this leaves a narrow band of the original color that represents locations with a tropopause potential temperature (θ) between 370 and 365 K. This process is repeated for subsequent isentropic levels down to the 260-K surface, resulting in a map that

depicts the distribution of potential temperature on the tropopause. Since the color bands simultaneously represent tropopause θ and upper-tropospheric PV, the two terms will be used interchangeably in what follows.

A much simpler technique would have been to interpolate potential temperature to the |PV| = 1.5 PVU surface directly and color fill the resulting two-dimensional grid. However, this method produces an aliased sawtooth pattern wherever the tropopause is discontinuous or folded (Morgan and Nielsen-Gammon 1998). The contour fill method preserves the smooth shape of the actual tropopause while depicting folds and discontinuities as jumps in the value of tropopause potential temperature.

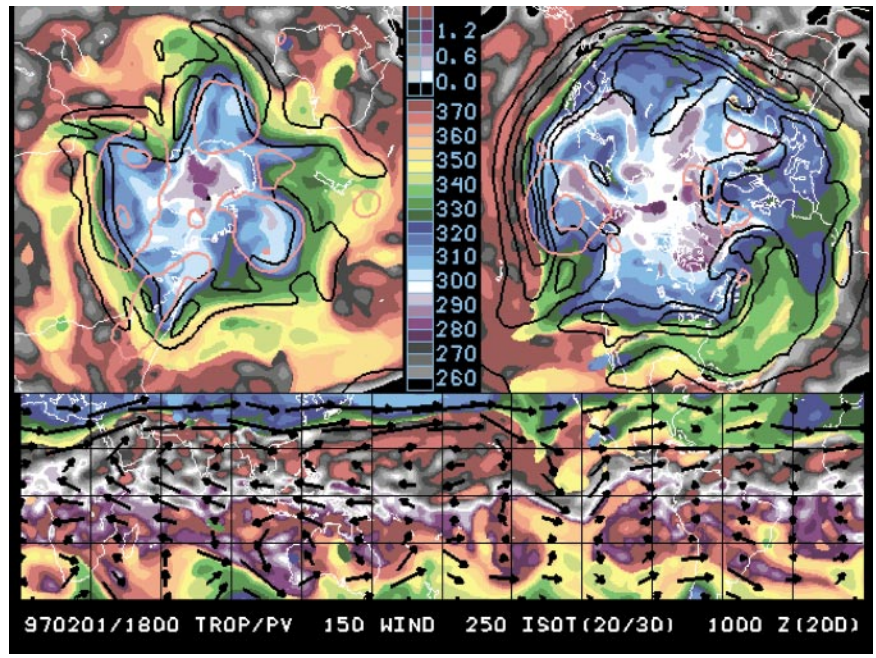

FIG. 1. Tropopause loop image from 1800 UTC 1 Feb 1997. Colors depict tropopause potential temperature (and 370-K potential vorticity near the equator); the scale is in the center of the figure. Black contours in the upper panels (left, Southern Hemisphere; right, Northern Hemisphere) are 250-mb wind speed at 20 m s^{-1} increments starting at 30 m s^{-1}. Red contours in the upper panels are 1000-hPa height contoured every 200 m for values of 0 m and below. Grid lines in the lower panel (Tropics) are every 20° of latitude and 30° of longitude. Black vectors in the lower panel are 150-hPa winds; a vector of 60 m s^{-1} spans 30° of longitude.

In tropical regions, PV is not an appropriate delineator of the tropopause (e.g., Hoerling et al. 1991; Hoinka 1998), since PV changes sign from one hemisphere to the other. In order to show equatorial upper-tropospheric dynamics, PV is contour filled between –1.5 and 1.5 PVU on the 370-K surface. The PV contours merge seamlessly with the tropopause potential temperature contours at the intersection of the ±1.5 PVU and 370-K surfaces, yielding a continuous depiction of upper-tropospheric PV over the entire atmosphere. The 370-K surface is close to the thermally defined tropical tropopause. According to Hoinka (1999), who used ECMWF reanalyses, the tropical tropopause averages about 366 K in the boreal winter and 360 K in the boreal summer, with the summertime tropopause as high as 380 K on average over the northeastern Indian subcontinent. Highwood and Hoskins (1998), using ECMWF *analyses,* obtained typical potential temperature values for the tropical tropopause of 372–380 K, with higher values again found over northern India. Gage and Reid (1987) found that the annual cycle of tropopause potential temperature for western tropical Pacific *rawinsondes* ranged between 367 and 376 K, highest in boreal spring and lowest in boreal summer.

c. Other aspects of the images

To show the entire globe, the image is broken up into three panels (Fig. 1). Along the bottom, the Tropics are represented by an equatorial band from 40°N to 40°S, with the Greenwich meridian at the left and right boundaries. The upper-left and upper-right panels depict the Southern and Northern Hemispheres, respectively, with polar stereographic projections aligned with the equatorial band beneath them.

Additional fields are overlaid onto the tropopause maps. In the equatorial band, the 150-hPa winds are shown by black vectors. The 150-hPa surface is just below the 370-K isentropic surface in the Tropics and tends to coincide with the poleward branch of the Hadley circulation (e.g., Johnson 1989, Figs. 8 and 9). In the extratropics, the wind speed at the 250-hPa layer is contoured in black at 20 m s^{-1} intervals starting at 30 m s^{-1} to show the jet stream configuration, and 1000-hPa heights of 0 m and below are contoured in red every 200 m to show the significant surface cyclones. The red contours are poorly visible in video format, but they are easily seen in the digital images. Geographical information is provided by continental

outlines (in white) on all panels and a 20° latitude by 30° longitude grid (in black) on the equatorial band.

d. Loop construction

The images were generated at 640 × 480 resolution in graphics interchange format (GIF) using a version of the General Meteorological Package (GEMPAK) enhanced with masking and maximum value grid functions. The images were then converted to cyan–magenta–black–yellow format, a black border was added, and the images were transferred to videotape with a dwell rate of five images per second. One month occupies about 20 s of loop time, and the entire 20-yr loop takes 84 min.

Six-hourly images were needed to produce the visual illusion of a continuously evolving field. When 12-h images were placed in a loop, the resulting loop appeared jerky, and the eye did not easily perceive the continuity of features from image to image. The smoothness of the 6-h loop suggests that tropopause PV features are preserved by the NCEP Global Data Assimilation System (Kanamitsu 1989; Kanamitsu et al. 1991; Kalnay et al. 1996) and are not subject to substantial modifications due to incorporation of sporadic observations in data-sparse regions. Aside from small-scale features in the PV field in the tropical upper troposphere, the tropopause maps appear to depict the actual state of the tropopause reasonably well.

3. Visualized dynamics

a. Jet streams

Jet streams are easily seen in the loop by the isotach contours at high latitudes and the wind vectors at low latitudes. Had wind not been plotted, the jet locations would still be apparent in the motion of small-scale tropopause potential temperature variations, which are advected by the larger-scale flow. Even a static image possesses information regarding the jet stream locations, since the jets typically correspond to strong gradients or discontinuities in tropopause potential temperature (Morgan and Nielsen-Gammon 1998).

Since one year occupies about 4 min of loop time, the annual variations in jet intensity, location, and structure are easily seen. Variations are much stronger in the Northern Hemisphere (NH) than in the Southern Hemisphere (SH); the NH summer jet is particularly anomalous, consisting of short, narrow jetlets that seem as likely to be oriented north–south as east–west. Figure 1 shows a typical NH wintertime pattern, while Fig. 2 shows a typical summertime pattern. Ranking the hemispheres by the size and intensity of the tropopause polar vortex, the NH winter vortex is the strongest, followed by the SH winter vortex, the SH summer vortex, and the NH summer vortex. The SH winter pattern tends to have a double-jet structure (e.g., Trenberth 1991), and the NH jet shows similar tendencies for separate polar and subtropical jets. The NH winter jet pattern in this instance can perhaps best be described as spiral, with the subtropical jet originating over Mexico, extending across northern Africa and southern Asia, becoming strong across the Pacific, continuing across central North America and the North Atlantic, and evolving into a series of high-amplitude troughs and ridges over northern Europe. This spiral pattern occurs frequently in the NH (R. L.Panetta 1997, personal communication).

The strong NH wintertime jet over the Pacific (Fig. 1) corresponds to a vertical or folded tropopause. Near the date line, a tropopause potential temperature discontinuity is present in

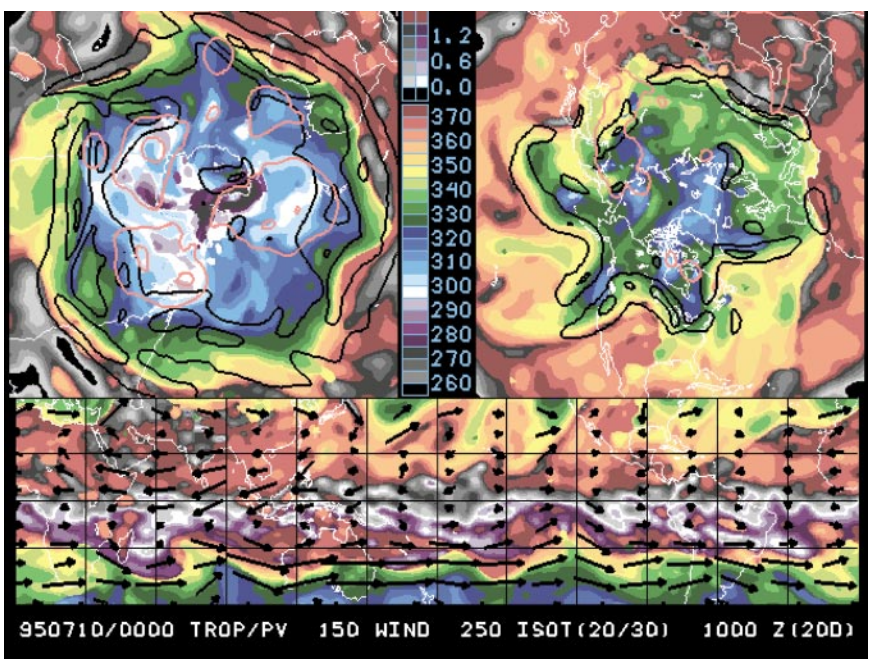

FIG. 2. Tropopause loop image from 0000 UTC 10 Jul 1995. As in Fig. 1 except for boreal summer.

which the tropopause jumps from 365 to 315 K. Such vertical tropopauses are common across the North Pacific in wintertime. In contrast, the only fully vertical tropopause associated with an NH summer jet in Fig. 2 is over southern Asia and is a product of upper-level outflow from the Indian monsoon.

Another notable difference between the two hemispheres is the degree of asymmetry in their circulations. The NH is known to have higher-amplitude planetary-scale waves than the SH, a fact attributed to the larger NH wave forcing from the topographic variations. The examples in Figs. 1 and 2 tell a slightly different story. The planetary-scale waves are not simply low-wavenumber displacements of PV, but represent fundamental differences in the PV distribution as one circles the globe. Over the western and central North Pacific in winter (Fig. 1), isentropic PV gradients are vertically stacked. Meanwhile, over the North Atlantic and Europe, two zones of isentropic PV gradients are present with a region of weak or reversed gradient in between. A similar zone of weak gradients is found over Europe and Asia in Fig. 2. The zones of concentrated and separated PV gradients might be expected to inhibit the north–south propagation of all but the longest planetary waves, since such waves would be evanescent in regions of zero PV gradients. The explanation of these fundamental gradient variations must involve small-scale eddies as well as large-scale forcing.

Interannual variability is also apparent in the upper-level jets. The most remarkable extratropical jets occurred during the winter of 1997/98, a strong El Niño period. Figure 3 shows the pattern for 1 February 1998, at which time the NH subtropical jet stream circled the globe at low latitudes. The NH circulation has rarely been so circularly symmetric. A rare fifth isotach appears in the jet off the west coast of North America, corresponding to wind speeds in the NCEP–NCAR reanalysis of 110 m s^{-1}. The wind speed maximum is collocated with a discontinuity in tropopause θ, signifying a tropopause fold that extends most of the way across the Pacific.

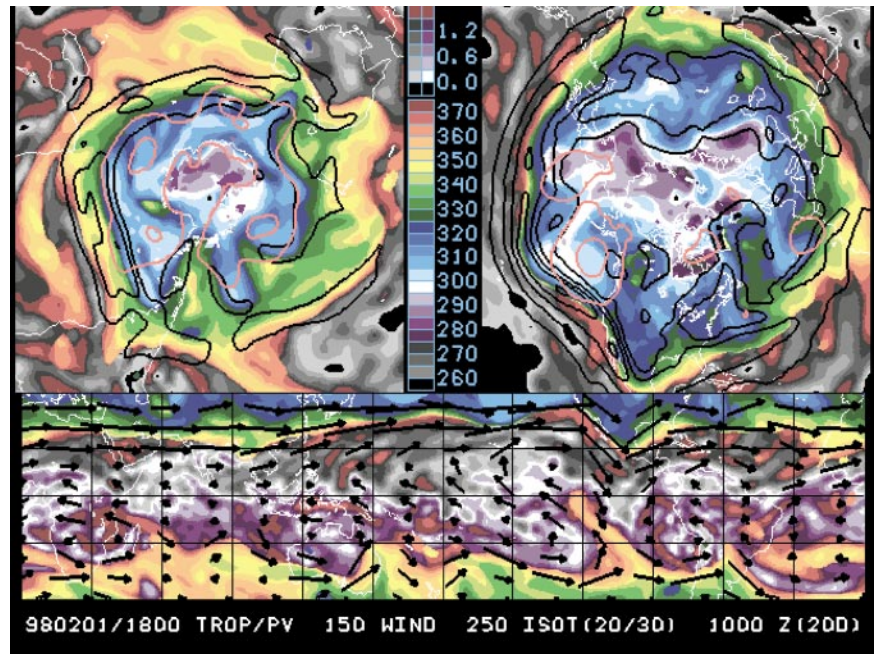

FIG. 3. Tropopause loop image from 1800 UTC 1 Feb 1998. As in Fig. 1 except for an El Niño year.

b. Waveguides

The strong potential temperature gradients (or discontinuities) along the jets represent waveguides along which Rossby waves can propagate. The different velocities of synoptic-scale waves along the jet stream compared to small-scale "debris" embedded in the jet dramatically illustrate the upstream phase velocity of Rossby waves.

Rossby wave packets and downstream development (Namias and Clapp 1944; Orlanski and Katzfey 1991; Chang 1993, 1999; Chang and Yu 1999) are easy to observe in the loop. They appear to be more common in the SH than the NH. It is frequently possible to trace a baroclinic wave packet most of the way around the hemisphere. A cyclogenesis event will amplify the upstream trough and downstream ridge. Farther downstream, a trough forms beyond the ridge and triggers a cyclogenesis event, and the cycle repeats.

An example of a high-amplitude Rossby wave packet that propagates halfway around the Northern Hemisphere is shown in Fig. 4. In the days preceding the first panel of Fig. 4, a cold tropopause anomaly ($\theta < 290$ K), corresponding to an intense upper-level trough, has moved southward from the Arctic toward the Asian jet. Along the jet, the tropopause θ varies abruptly from 300 to 365 K, signifying a strong, concentrated PV gradient that can support Rossby waves.

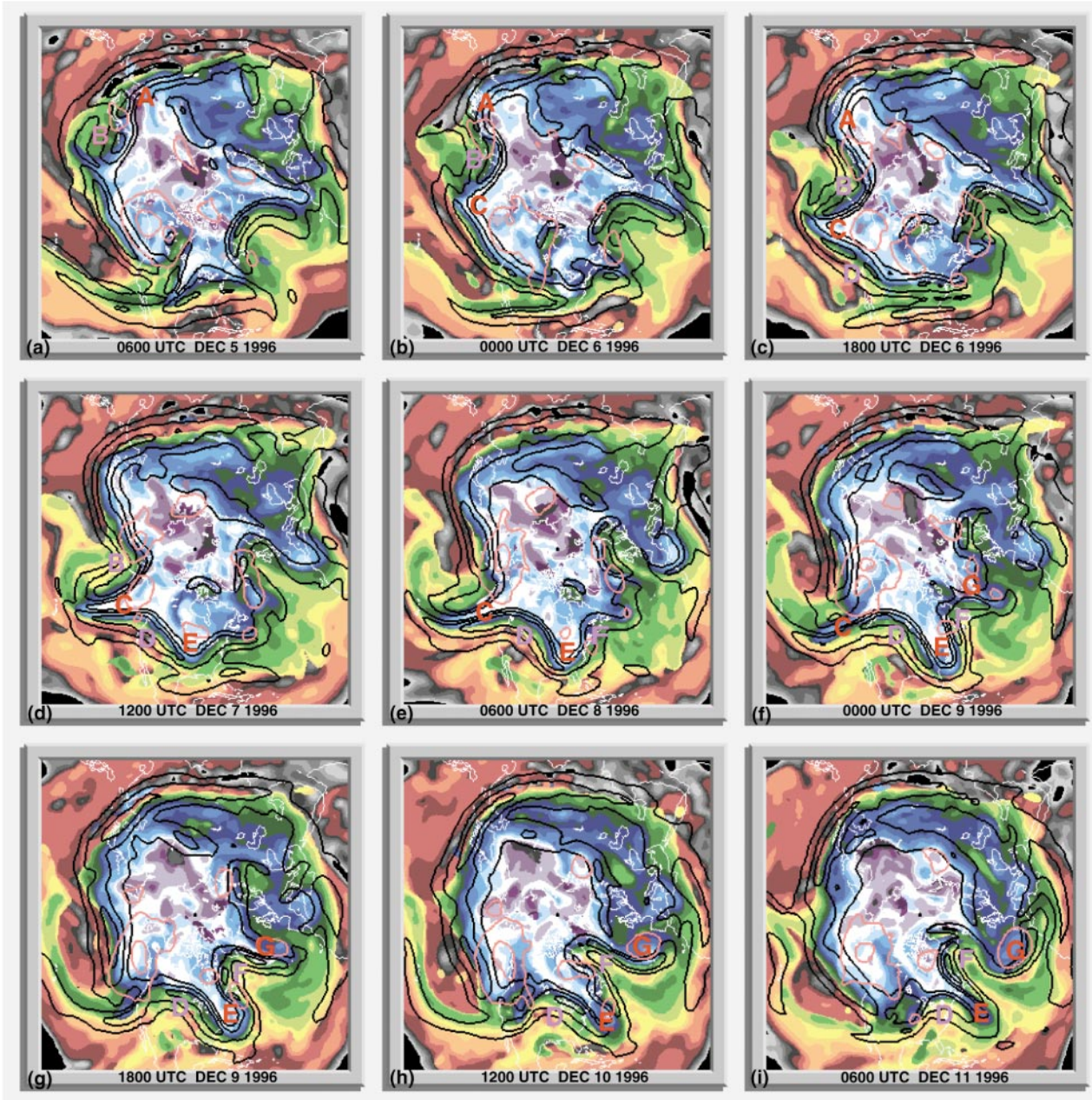

FIG. 4. (a)–(i) Northern Hemisphere panels from the period 0600 UTC 5 Dec through 0600 UTC 11 Dec 1996, at 18-h intervals. Plotting conventions as in Fig. 1; labels A–G indicate successive troughs and ridges in a Rossby wave packet.

As the anomaly reaches the jet, the cyclonic circulation associated with the anomaly induces a wave along the PV gradient, with a ridge to the east of the anomaly and a trough to its west (Nielsen-Gammon 1995). The trough is labeled A and the ridge labeled B in Fig. 4a, and the anomaly that induced them lies between them, shaded purple.

Were this the only source of wave energy, this might be the end of wave amplification. But a surface cyclone has developed simultaneously with the trough–ridge couplet. This cyclone is indicated by the red contour centered over northern Japan. Its presence midway between the trough and the downstream ridge implies a configuration favorable for the conversion of available potential energy into eddy kinetic energy. This provides an additional important energy source for downstream development of the wave packet (Orlanski and Katzfey 1991; Chang 2000). Thus, 18 h later (Fig. 4a), the trough, ridge, and surface cyclone have all intensified, and a new trough (labeled C) has

appeared downstream of the ridge. From a PV perspective, this trough has formed by PV advection associated with the northerly winds located downstream of the anticyclonic PV anomaly B (Nielsen-Gammon and Lefevre 1996). In a dynamical context, trough C is an individual wave at the leading edge of a Rossby wave packet consisting of A, B, and C.

Just as a ridge begets a downstream trough, a trough begets a downstream ridge, as long as the PV distribution allows for wave growth. Ridge D first appears in Fig. 4c, trough E in Fig. 4d. As it moves along, the wave continues to extract energy from the background shear, as suggested by the small cyclone that appears between trough C and ridge D in Fig. 4d and the cyclone that appears between trough E and newly formed ridge F in Fig. 4e. Our designation of the formation times of these troughs and ridges is subjective and somewhat arbitrary, but the overall evolution is robust. It is clear (for example) that trough E, which attains high amplitude over the east-central United States at 0600 UTC 8 December 1996 (Fig. 4e), did not even exist 54 h earlier (Fig. 4b). Someone focusing on North America might conclude that trough E was a new development, while according to a more global viewpoint the energy of trough E was already present in troughs A and C and was well on its way to North America 54 h earlier.

Heretofore the tropopause θ gradient at the leading edge of the Rossby wave packet has been strong and localized, a medium well suited for supporting waves. The situation changes as the wave packet crosses North America; over Europe, the latitude of the Rossby wave packet is marked by homogenized tropopause θ of about 320 K, with concentrated gradients displaced well to the north and south. Thus, while trough G forms on schedule, there is no subsequent development of a ridge H. Instead, trough G rapidly amplifies, breaks, and forms a cutoff PV anomaly vertically superposed with its associated surface cyclone. By the end of the sequence it appears that cutoff G is far enough south to begin triggering a wave along the subtropical jet, but for our purposes cutoff G represents the end of the wave packet.

Meanwhile, by the end of this time period, features A–C have disappeared. Just as waves form on the leading edge of a Rossby wave packet, waves dissipate on the trailing edge of a Rossby wave packet. For example, trough C is near the leading edge of the wave packet in Figs. a–c, and the ridge upstream of C is stronger than the downstream ridge. Because of the difference in amplitude of the two ridges, the northerlies associated with B at the trough's location should be stronger than the southerlies associated with D, resulting in net northerlies within trough C and consequent amplification. By Fig. 4d trough C is near the center of the wave packet, the upstream and downstream ridges are similar in strength, and the winds associated with the two ridges should cancel at the trough location. At this time trough C is at its strongest. In Figs. 4e and f trough C is near the trailing edge of the wave packet, the southerlies associated with ridge D are stronger than the northerlies associated with ridge B, and trough C weakens. Of course, trough C has had its own impact; its associated northerlies helped to weaken upstream ridge B and its associated southerlies helped to strengthen downstream ridge D.

Not all the energy generated by baroclinic amplification propagates downstream; some leads to Rossby wave breaking and the ultimate return of some energy to the mean flow. Troughs C, E, and G all break, but they break in quite different ways. Trough C resembles the anticyclonic LC1 life cycle of Thorncroft et al. (1993), with a long PV streamer stretched anticyclonically toward the subtropics. By 1200 UTC 10 December 1996, the streamer reaches more than halfway across the Pacific. Meanwhile, in Figs. 4g and h, there is a hint of secondary cyclogenesis associated with the remnants of trough C over the northwestern United States, which is also reminiscent of the idealized life cycle in Thorncroft et al. Trough G breaks in the manner of the cyclonic LC2 life cycle of Thorncroft et al., with the breaking wave forming a pronounced, symmetric cutoff low equatorward of the jet. Thorncroft et al. obtained these different life cycles by varying the background barotropic shear; inspection of Fig. 4 reveals the presence of a subtropical jet south of trough G and the absence of a subtropical jet south of trough C, consistent with enhanced cyclonic shear for the trough G life cycle. Trough E occupies an intermediate location both geographically and dynamically, breaking neither cyclonically nor anticyclonically but becoming elongated from Hudson's Bay to well south of Bermuda. Hartmann and Zuercher (1998) found that the transition from cyclonic to anticyclonic life cycle behavior is abrupt, so that troughs like trough E would be seen only rarely, but they based this conclusion on behavior 3–5 days after the waves had attained maximum amplitude in a periodic domain. The finite spatial and temporal lengths of real wave packets such as this one probably make it unlikely that individual waves will survive long enough to produce the clear, abrupt transition in behavior found in the idealized model.

c. Wave breaking

Wave breaking and spinup of small-scale vortices is a frequent occurrence, particularly in the SH. Over the course of about two days, as with trough C in Fig. 4 above, a wave will become elongated toward the equator (anticyclonic wave breaking is comparatively rare) and will be stretched to a width of about 300–500 km. The entire tropopause filament may continue to narrow and ultimately become unresolved by the analyses, but more commonly the trailing end of the filament will wrap up into a vortex. Additional vortices sometimes form along the filament. The evolution closely resembles contour dynamics simulations of wave breaking in the stratosphere, down to the details of the interactions of the breaking wave and vortex with successive waves in the jet stream.

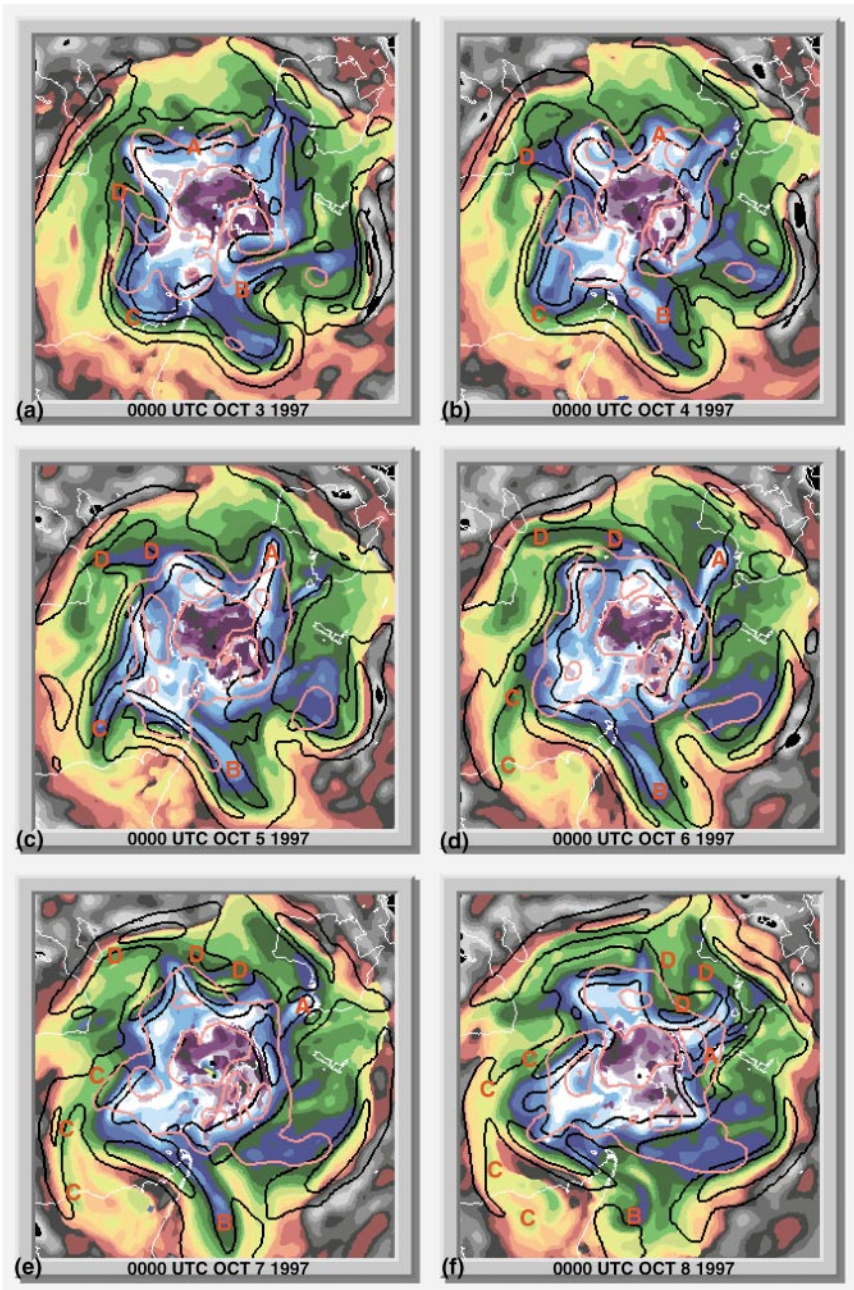

FIG. 5. (a)–(f) Southern Hemisphere panels from the period 0000 UTC 3 Oct through 0000 UTC 8 Oct 1997, at 1-day intervals. Plotting conventions as in Fig. 1; labels A–D indicate breaking Rossby waves.

An SH event with several simultaneous trough wave breaking events is shown in Fig. 5. In Fig. 5a, the four troughs are labeled A–D. Trough A forms a closed PV center that is subsequently drawn poleward and stretched meridionally ahead of the next trough. Trough B forms a thicker PV streamer that ultimately wraps up cyclonically into the shape of an inverted comma. Trough C curves anticyclonically equatorward of the jet (like trough C in Fig. 4), possibly breaking up into several vortices, although the resolution of the reanalysis dataset makes the evolution ambiguous. Finally, trough D extends anticyclonically equatorward as well, but its PV streamer interacts with a subsequent trough so that a portion of the streamer is drawn poleward into the developing ridge. Again, the resolution of the reanalysis data makes it difficult to track the streamer after it thins.

The modes of wave breaking manifested by these four troughs are similar to the wave breaking events found throughout the 20-yr dataset. They also appear remarkably similar to idealized contour dynamics simulations of wave breaking. For example, the evolution of troughs A, B, C, and D in Fig. 5 appear to correspond to the wave breaking events shown in Figs. 15, 4, 14, and 10, respectively, of Polvani and Plumb (1992). Polvani and

Plumb were simulating a stratospheric vortex perturbed by topographic forcing by representing the PV distribution as two uniform PV regions separated by a discontinuity. Differing modes of wave breaking were obtained by Polvani and Plumb by varying the amplitude of the waves with a single PV discontinuity, but their results with a five-contour model do not resemble wave breaking in the tropopause loop so closely. Apparently the concentrated gradients associated with the jet streams along the tropopause are more appropriately modeled in this context as a zero-order discontinuity of potential vorticity than as a broader PV gradient.

d. Anticyclonic PV plumes

Another dramatic sort of evolution that takes place in either hemisphere is what we shall call anticyclonic PV plumes. In certain regions of the subtropics such as Southeast Asia, central South America, central Africa, and northern Australia, stationary upper-level closed anticyclones are present during part of the year, being diabatically driven by deep convection. Frequently, a streamer of anticyclonic PV will be drawn out of the anticyclonic reservoir and extend along the adjacent jet. Such plumes can sometimes extend thousands of kilometers.

One such plume may be seen in Fig. 4. In Fig. 4b, even as ridge B grows, trough A impinges upon the very warm tropopause air ($\theta > 360$ K) of the subtropics. This air is drawn northeastward along the jet toward ridge B in a long, narrow streamer. By Fig. 4e the warm, low PV air begins to roll up anticyclonically at its leading edge, and the leading anticyclonic rollup continues to grow in size through Fig. 4h. The evolution of the plume may be contrasted with ridge F in the same figure, which resembles an anticyclonic version of the wave breaking discussed above. The North Pacific is a common location for these anticyclonic plumes, perhaps because the subtropical air is found in close proximity to polar mobile troughs and a strong jet over eastern Asia and the western North Pacific. It appears that the breaking of trough C is caused in part by the presence of this anticyclonic plume.

Three more anticyclonic plumes are shown in an example from the SH in Fig. 6. Plume A originates over Argentina, equatorward of an intense upper-level trough and surface cyclone. The anticyclonic plume is drawn eastward across the Atlantic along the southern edge of the jet, eventually rolling up anticyclonically over South Africa in Fig. 6f. Plume B forms to the west, ahead of another large-scale trough. The development and rollup of plume B occurs synchronously with plume A, the only major difference being that the tropopause θ associated with plume B is about 25 K colder. Plume C is triggered over Australia by a smaller-scale trough, resulting in a narrower anticyclonic streamer that first forms an anticyclonic rollup at its leading edge in Fig. 6e.

In Fig. 6e and f (and probably in subsequent panels as well), the leading edge of plume C is obscured by higher PV air beneath it, plotted as green in the figure. The tendency of these anticyclonic plumes to be stretched out horizontally and ultimately be surrounded by air with stratospheric values of PV suggests that they may be an important mechanism for the irreversible transport of air from the subtropical troposphere to the lower stratosphere [see the introductory discussion in Vaughan and Timmis (1998)], although this mechanism seems somewhat different from the higher-latitude anticyclonic wave breaking events (such as ridge F in Fig. 4) studied by Peters and Waugh (1996), Vaughan and Timmis (1998), and O'Connor et al. (1999). In most cases, the rolled-up anticyclones remain adjacent to the jet and gradually slow. The exception of this pattern of motion is found with anticyclones that break off from the west side of the Indian monsoon anticyclone; these anticyclones initially move westward before being picked up by the westerly subtropical jet across central Asia (Hsu and Plumb 2000).

Another common characteristic of anticyclonic plumes is that they tend to be bounded on their poleward side by a jet streak. This can be seen in all four plumes discussed above. This behavior would be expected from static PV balance arguments, since along the poleward side of an anticyclonic plume the PV jump across the jet is locally enhanced. However, as seen in the examples, the tropopause potential temperatures poleward of the plumes also tend to be colder than surrounding values of θ, further enhancing the cross-jet PV jump. This may be related to the means of formation of anticyclonic PV plumes, which in the examples are initiated when unusually cold tropopause air extrudes southward toward the jet. The extent to which long-lived jet streaks may be related to such plumes is a subject that merits further research.

e. Cyclogenesis

Cyclogenesis is visualized in the individual images through contours of 1000-hPa height wherever the height values are zero or negative. Even absent such height contours, strong cyclogenesis events typically

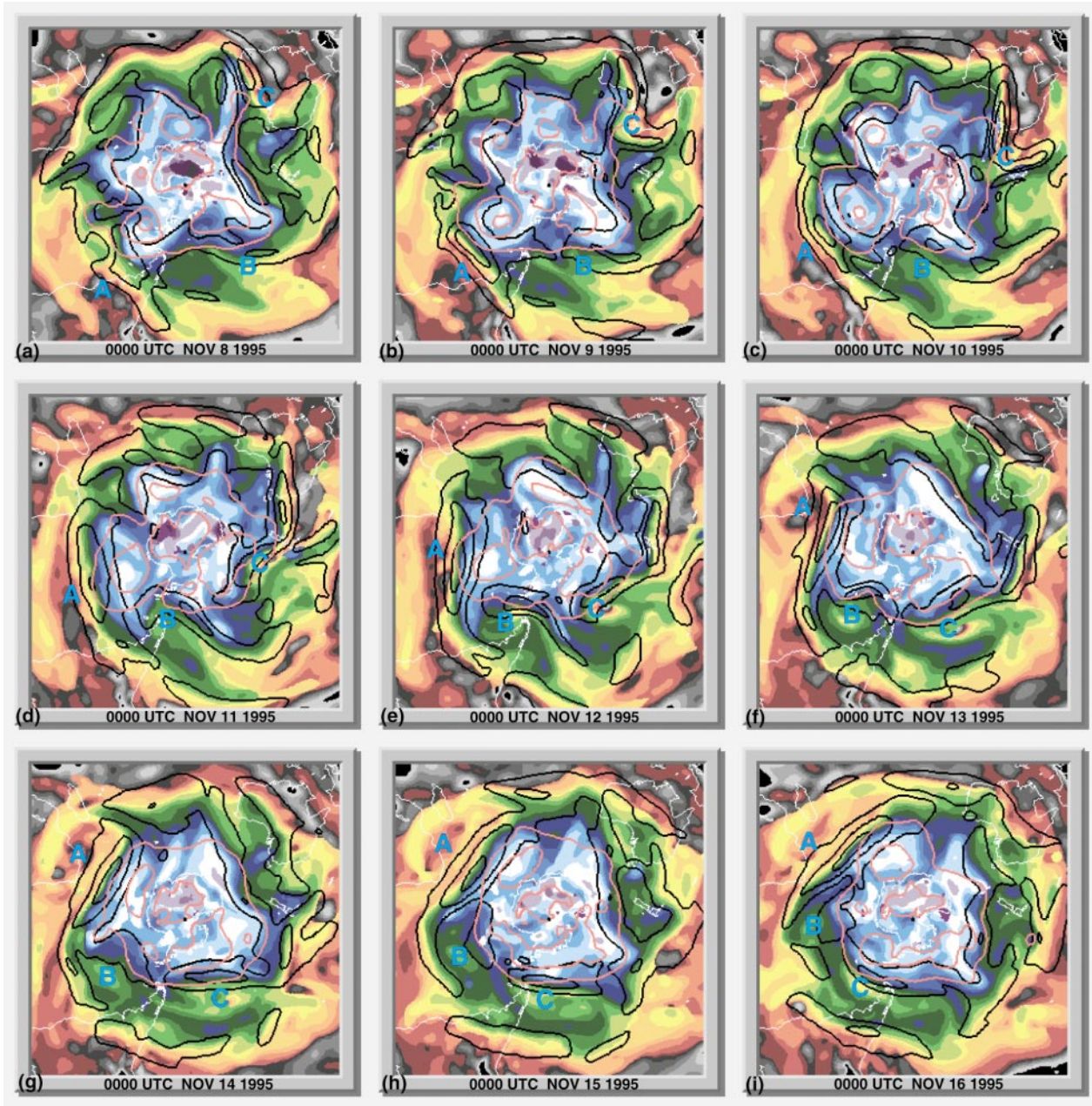

FIG. 6. (a)–(i) Southern Hemisphere panels from the period 0000 UTC 8 Nov through 0000 UTC 16 Nov 1995, at 1-day intervals. Plotting conventions as in Fig. 1; labels A–C indicate anticyclonic PV plumes.

are marked at the tropopause by the cyclonic wrapup of PV. These structures develop over the course of 1–2 days and have been called bell-and-clapper (Bosart et al. 1996) or treble clef (Martin 1998) patterns.

Two of the most rapidly deepening storms over North America during the period of the loop were the "Cleveland Superbomb" of 1978 (Salmon and Smith 1980; Hakim et al. 1995, 1996) and the "Storm of the Century" of 1993 (Kocin et al. 1995; Huo et al. 1995; Bosart et al. 1996). The two storms are shown in Fig. 7 in order to illustrate the structure of the tropopause map during rapid cyclogenesis and to show how similar the two events were. Upper-level potential vorticity maps of the full evolution of the 1978 event have been presented by Hakim et al. (1995), and tropopause maps of the full evolution of the 1993 event have been presented by Bosart et al. (1996).

Both storms involved the merger of two upper-level disturbances, which are indicated by the dark blue arrows in the top panels of Fig. 7. The northern

disturbances are marked by very cold tropopause potential temperatures. The southern disturbances, while cold for their latitude, are 20–25 K warmer than the northern disturbances. This mismatch of tropopause θ may be particularly favorable for rapid cyclogenesis because it enables the two disturbances to become vertically stacked, maximizing their combined circulation.

In Figs. 7c and d, the northern disturbances have advected rapidly southward and are in the process of merging with the southern disturbances. This rapid southward motion may be interpreted from a PV perspective as being due to the prominent anticyclonic PV (warm tropopause) anomalies immediately to the west of each northern disturbance, combined with the absence of anticyclonic PV anomalies immediately to their east. The asymmetry produces a strong northerly jet that carries the cyclonic anomaly southward, intensifying it, and also carries the anticyclonic anomaly southward, weakening it. At the time of Figs. 7c and d, the cyclones are already rapidly intensifying, and the first red contours (indicated by the blue arrows, and signifying 1000-hPa heights below 0 m) have appeared downstream of the troughs. In the 1978 case the initially positively tilted combined trough has become negatively tilted, while in the 1993 case the original negative tilt has increased.

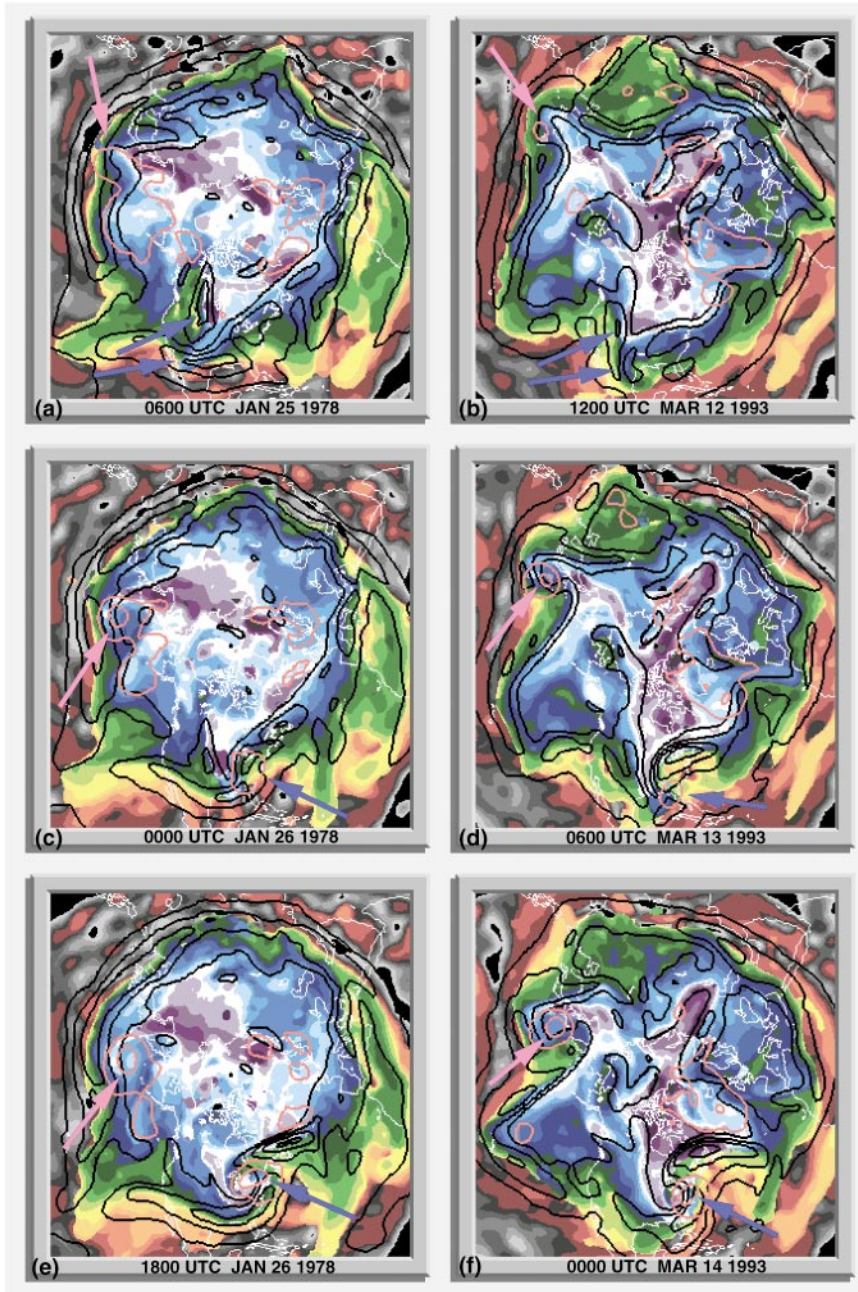

FIG. 7. (a)–(f) Northern Hemisphere panels from the period 0600 UTC 25 Jan–1800 UTC 26 Jan 1978 (left column, the Cleveland Superbomb) and from 1200 UTC 12 Mar to 0000 UTC 14 Mar 1993 (right column, the Storm of the Century), at 18-h intervals. Plotting conventions as in Fig. 1; see text for meaning of arrows.

In Figs. 7e and f, only 18 h after the middle panels, the upper-level disturbances have merged and wrapped up cyclonically in a dramatic spiral pattern. The surface lows have also intensified, as indicated by the appearance of a second red contour. The centers of the surface circulation are displaced to the east from the center of the upper-level cyclonic wrapup. The upper-level wind patterns are also remarkably similar: one jet core, in excess of 70 m s^{-1}, extends along the southern perimeter of the upper-level disturbance and curves cyclonically along its eastern edge, while a second jet core, in excess of 90 m s^{-1}, is oriented NW–SE downstream of the cyclone. If one were to trace the axes of the jets, one would find a pattern very similar

to the surface frontal distribution of a developing cyclone. The two jets agree with the classic jet configuration for East Coast snowstorms (Kocin and Uccellini 1990, 60–63), although it is clear that much of the intensity of the northern jet is due to low PV aloft (warm tropopause θ) generated by diabatic processes during the cyclogenesis itself and ageostrophic accelerations associated with the rapid upward motion (see, e.g., Bosart et al. 1996; Cammas et al. 1999). The sudden appearances of light green shadings downstream of the 1978 storm and yellow shadings downstream of the 1993 storm imply nonconservation of PV associated with midtropospheric diabatic heating.

Almost as if to confirm that the cyclonic wrapup is not limited to exceptional events, similar upper-level developments associated with single trough cyclogenesis events take place over the Pacific Ocean (pink arrows) during both events.

f. The tropical tropopause

The tropical tropopause is a quite different place than the midlatitude tropopause. One key difference is the distribution of PV gradients (and potential temperature gradients on the tropopause) and the associated propagation characteristics of Rossby waves. While PV variations are present, they tend to be local in nature, and most of the globe within 20° of the equator has little systematic PV gradient and no apparent propagation of Rossby waves. The only exception is the PV gradient that is established during the boreal winter over the eastern Pacific, corresponding to the so-called cross-equatorial wave duct (Webster and Holton 1982; Tomas and Webster 1994). A typical example of such a gradient is shown in Fig. 1. While waves are frequently apparent along this gradient, there is little or no visual evidence of wave energy propagating through the Tropics along the tropopause, although such waves do show up in bandpass correlation analyses (e.g., Tomas and Webster 1994).

The annual cycle of midlatitude jets is a prominent aspect of the loop. Even more prominent, however, is the less familiar annual cycle in the tropical tropopause. It is not surprising that there are local increases in the potential temperature of the tropopause during seasonal tropical convection, but a more widespread variation takes place over the equatorial Pacific. The NH tropical tropopause has its highest potential temperature during winter and spring and its lowest potential temperature during summer. This effect is concentrated over the oceans, particularly the subtropical Pacific (cf. Figs. 1 and 2), and is consistent with annual variations in low-level equivalent potential temperature (Reid and Gage 1981).

The seasonal variations in tropical North Pacific tropopause height have been extensively documented and discussed by Reid and Gage (1996). The tropopause potential temperature variations in this loop are consistent with those height variations and with the potential temperature variations found by Highwood and Hoskins (1998) and Hoinka (1999). The exact cause of this annual fluctuation has not been determined; Reid and Gage (1996) attribute it to a combination of extratropical wave driving and tropical convection.

Another prominent annual cycle is the Asian monsoon. The monsoon is manifested in the tropopause loop in two ways. First, a prominent anticyclone develops rapidly and nonconservatively (Hoskins 1991) in the form of a tropopause potential temperature maximum over the northern Indian subcontinent and Tibet (Fig. 2). The monsoon anticyclone has a typical east–west dimension of 4000–6000 km and a north–south dimension of 2500 km. Occasionally, as described in section 3d, large pieces of the anticyclone are shed to the west and move to the west and north.

The second manifestation of the monsoon cycle is the development of the tropical easterly jet stream over the northern Indian Ocean and northern Africa. This jet, which is remarkably unperturbed by wavelike disturbances, develops in early June at the same time as the Indian anticyclone at a latitude of about 10°. The entrance and exit regions of this jet are areas of strong deformation, as tropopause potential temperature anomalies are drawn into the jet from the tropical North Pacific and are ejected over the tropical North Atlantic. The entrance region has been studied recently by Postel and Hitchman (1999), who declared it a region of Rossby wave breaking because the northward PV gradient becomes negative there. However, the mean PV gradient north of the jet is necessarily negative on average throughout the season to support the strong easterlies of the jet, so it is not clear to what extent the gradient reversals relate to ordinary wave breaking.

The standard version of the secondary tropical circulation consists of a seasonally varying pair of Hadley cells, with strong upward motion on the equator and strong downward motion on the winter side of the equator. In the global visualization it is apparent that this zonally symmetric view of the Hadley circulation bears scant resemblance to the actual flow patterns near the tropopause in the equatorial region at any

given time. The Hadley circulation is most easily seen in the loop along the equator, where it is possible to infer net cross-equatorial transport and consequently to diagnose the upper branch of the Hadley circulation.

A typical snapshot is shown in Fig. 2. Since this is during boreal summer, the expected cross-equatorial transport aloft is from north to south. A net north–south transport is indeed observed, but is seen to be concentrated in a narrow latitude band between 60° and 120°E. Over the rest of the equator, there is little or no cross-equatorial transport. The situation is similar during boreal winter (Fig. 1), except in this instance the primary cross-equator transport (from south to north) is between 30° and 90°E. These images illustrate the general tendency for the upper portions of the Hadley circulation to be confined to a small fraction of the equatorial domain.

g. Hurricanes and extratropical transitions

Hurricanes are not among the features intended to be visualized through tropopause maps. They appear because the stratosphere is assumed to include any air above 650 hPa with an absolute value of PV greater than 1.5 PVU. The strongest hurricanes and typhoons generate strong and deep columns of diabatically generated PV (e.g., Shapiro and Franklin 1995) that frequently exceed this threshold and appear as (usually) green vortices within an otherwise very high-θ tropopause.

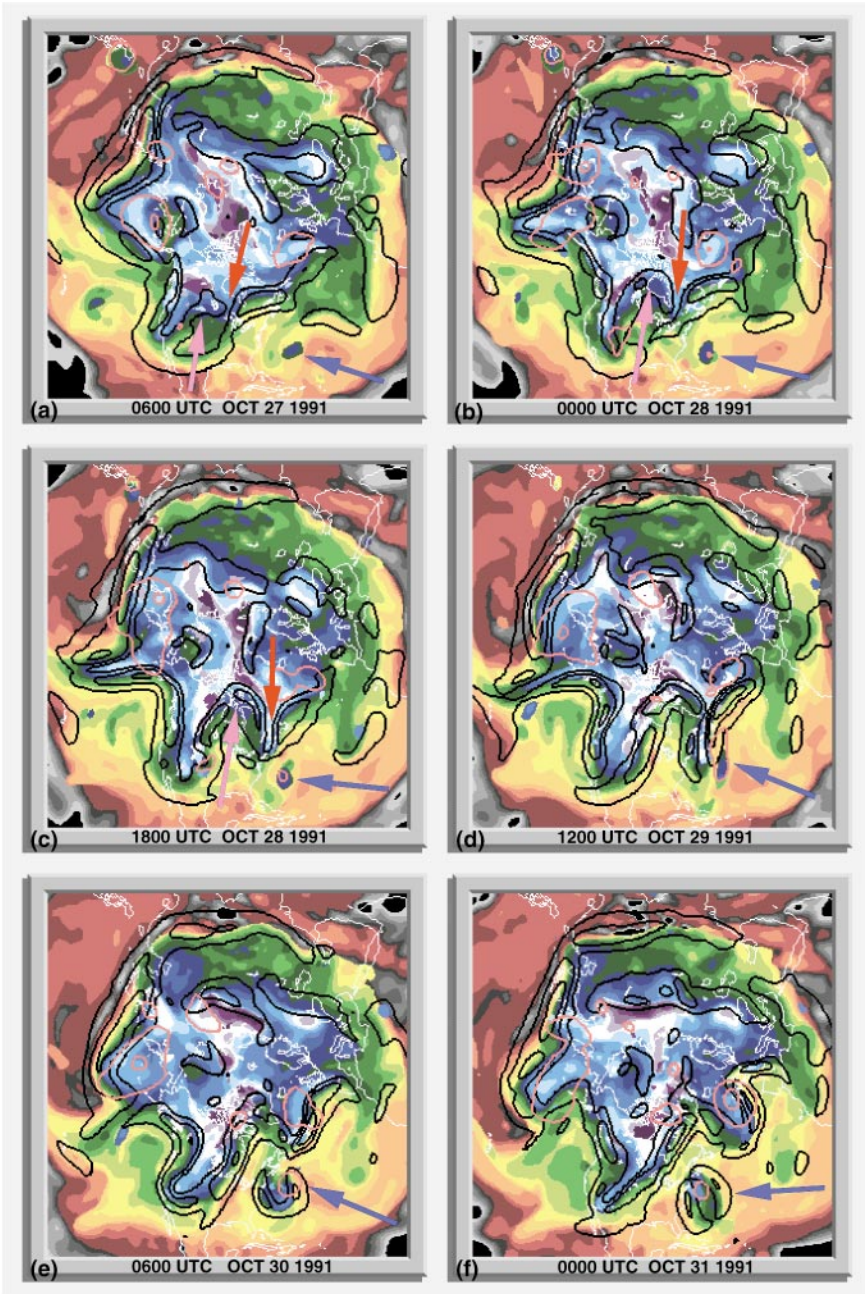

FIG. 8. (a)–(f) Northern Hemisphere panels from the period 0600 UTC 27 Oct through 0000 UTC 31 Oct 1991, at 18-h intervals. Plotting conventions as in Fig. 1; red arrow indicates developing trough, pink arrow indicates upstream developing ridge, and blue arrow indicates potential vorticity initially associated with Hurricane Grace and later with the "Perfect Storm."

Apart from the entertainment value of watching strong tropical cyclones traverse the oceans and make landfall, the tropopause visualization also shows many interesting dynamical aspects of the transformation of tropical cyclones into extratropical weather systems. An outstanding example of this phenomenon is the "Perfect Storm" (Junger 1997) or "Halloween storm" (Cardone et al. 1996) of October 1991 (Fig. 8). In Fig. 8a, Hurricane Grace (blue arrow) appears as a dark blue and green blob near Bermuda. The colors imply that the 325- and 330-K surfaces are above the 650-hPa

level and contain PV greater than 1.5 PVU. It is likely that the large horizontal scale of the high PV is an artifact of the low resolution of the analysis; the true isentropic PV distribution about Hurricane Grace is probably more compact and more intense.

The other players in the event are a weak upper-level trough (red arrow) and an upstream ridge (pink arrow). The ridge grows rapidly between 27 and 29 October; by Fig. 8d tropopause potential temperatures in excess of 340 K extend to northern Hudson's Bay. While a detailed analysis of this ridge development is beyond the scope of this paper, it appears that its growth is a combination of downstream development (note the high-amplitude trough and ridge upstream that also amplify), cyclogenesis (note the red contour, signifying an intense surface cyclone, over the central United States in Figs. 8a–c), and diabatic heating (note the rapid expansion of tropopause θ values between 340 and 360 K). Whatever the cause of the ridge amplification, it is almost unavoidably followed by downstream trough amplification as discussed in section 3b. In this case, the amplification of the trough appears to also be aided by the growth of the downstream ridge, which itself is probably aided by the upper-level outflow from Hurricane Grace.

Whatever the specific mechanisms, the upper-level trough and the hurricane are on a collision course by the time of Fig. 8c. Grace has developed a closed red contour, indicating 1000-mb heights below 0 m at the resolution of the analysis. From this point onward, the situation evolves rapidly. Figure 8d shows that the trough has begun to cut off from the polar high PV reservoir and the PV remnants of Grace have begun to stretch north–south under the influence of the nearby upper-level trough. The 0-m contour has a double-lobed structure suggestive of the merger of the extratropical and tropical cyclones that is about to take place. By Fig. 8e, all tropopause potential temperatures below 330 K have cut off from the polar vortex, and the upper-level jet around the cutoff has become nearly circular. Finally, in Fig. 8f, the entire system has become almost perfectly symmetric, with matching banana-shaped jets to the east and the west of the upper-level cutoff and a surface cyclone located directly beneath the center of the upper-level cutoff.

h. El Niño and La Niña

Because a year occupies 4 min of the loop, it is not easy to perceive interannual variations associated with such phenomena as the El Niño–Southern Oscillation (ENSO) cycle. However, the global circulation changes associated with ENSO are associated with substantial PV changes and consequently appear in the visualization as changes in the potential temperature and winds at the tropopause.

Figure 3 was a plot of the global tropopause in boreal winter during a strong El Niño event, while Fig. 1 was a plot during a neutral period. For comparison, Fig. 9 shows the equatorial band during two other years: one a strong El Niño, the other a strong La Niña. The difference in the equatorial tropopause is dramatic. During El Niño, the PV of the 370-K surface over the tropical North Pacific is almost entirely less than 1.5 PVU; during La Niña, the 370- and 365-K surfaces are greater than 1.5 PVU except directly along the equator and over the Maritime Continent. As Arkin and Webster (1985) and Tomas and Webster (1994) have noted, the upper-tropospheric westerlies in the eastern tropical Pacific are weak or nonexistent during El Niño events, inhibiting cross-equatorial propagation of stationary Rossby waves. The tropopause maps show that, in addition to a weakening of the westerlies, El Niño also brings a weakening of the cross-equatorial PV gradient in the upper troposphere, making cross-equatorial propagation of any Rossby waves in the upper troposphere especially unlikely.

Previous studies of changes in the potential temperature of the boreal winter tropical tropopause during El Niño (Gage and Reid 1986, 1987) have found that the tropopause θ increases over the western tropical Pacific and decreases over the eastern tropical Pacific. A more recent study using both rawinsonde and NCEP–NCAR reanalysis data (Randel et al. 2000) examined tropopause pressure and temperature variations; using this data to compute tropopause potential temperature, we find that Randel et al.'s climatology confirms the drop in tropopause θ over the eastern tropical Pacific during El Niño while changes in tropopause θ over the western tropical Pacific are not significantly different from zero. In contrast, the tropopause loop shows little change of tropopause θ in the western tropical Pacific but significant warming over the eastern tropical Pacific. Since both the Randel et al. (2000) study and the present study use NCEP–NCAR reanalysis data over similar periods, the apparently conflicting results must be related to differences in the definition of the tropopause. Randel et al. (and Gage and Reid) use a lapse rate definition, while our maps show potential vorticity, a function of both lapse rate and vorticity. Indeed, the vorticity contrast in Fig. 9 over the eastern tropical Pacific (between

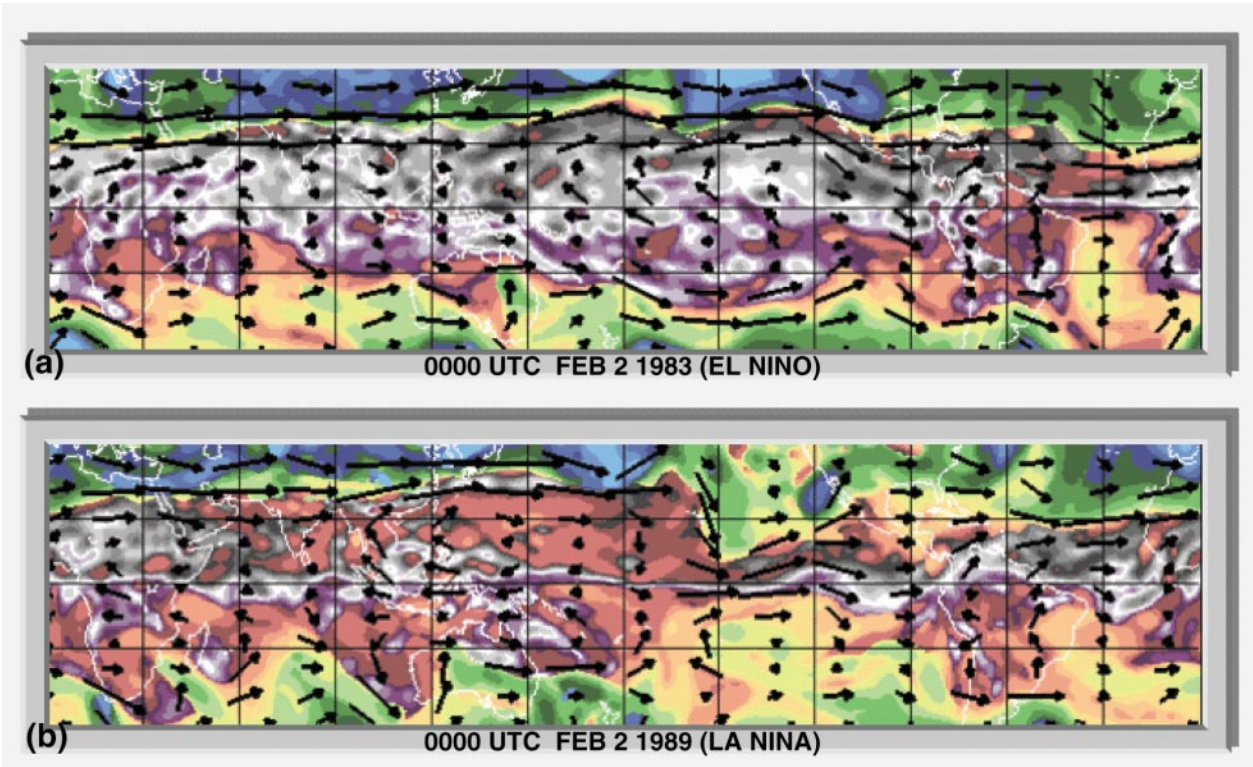

FIG. 9. Tropical panels from 0000 UTC 2 Feb of an El Niño year (top, 1983) and a La Niña year (bottom, 1989). Plotting conventions as in Fig. 1.

120° and 150°W) is even more dramatic than the tropopause θ contrast, with anticyclonic relative vorticity at 150 hPa everywhere between 30°N and 30°S in the El Niño year and cyclonic relative vorticity everywhere between 30°N and 30°S in the La Niña year. Two lessons from Highwood and Hoskins (1998) come to mind: first, that different definitions of the tropopause relate to different physical processes such that no single definition is always "correct"; second, that there is much about the dynamics of the atmosphere in the tropical upper troposphere that remains to be understood.

4. Summary

We have described a 20-yr visualization of the global tropopause. This visualization presents observed dynamical aspects of a variety of midlatitude and tropical weather phenomena, as well as features of the general circulation. The visualization videotape is useful as a research tool, as it presents a novel and dynamically appealing way of viewing common features of the global circulation, as well as strikingly illustrating some less widely known aspects such as anticyclonic PV plumes and the annual cycle of the tropical tropopause. The visualization videotape is also useful as a teaching tool, as it allows students to develop an intuitive conceptual model of potential vorticity, Rossby waves, jet streams, and the Hadley circulation based on the real atmosphere rather than simplified interpretations of the real atmosphere.

Selected individual images are posted online (http://www.met.tamu.edu/tropopause). The images are in GIF format; each image is 60–70 kb and the complete set of images for 20 yr and 4 months is approximately 3 Gb. No loops are posted at the Web site, but users are encouraged to construct their own short loops using programs with animation capabilities.

Copies of the videotape are available from the author for the cost of reproduction and mailing. To request one or more videotapes, visit the Web page or contact the author at the address given on the title page of this article.

Acknowledgments. This work, including creation of the videotape loop, was funded by the National Science Foundation through Grants ATM-9521383 and ATM-9553284. The master videotape was created from the individual images by the Visualization Laboratory within the College of Architecture at Texas A&M University.

References

Arkin, P. A., and P. J. Webster, 1985: Annual and interannual variability of tropical–extratropical interaction: an empirical study. *Mon. Wea. Rev.,* **113,** 1510–1523.

Bosart, L. F., G. J. Hakim, K. R. Tyle, M. A. Bedrick, W. E. Bracken, M. J. Dickinson, and D. M. Schultz, 1996: Large-scale antecedent conditions associated with the 12–14 March 1993 cyclone ("Superstorm '93") over eastern North America. *Mon. Wea. Rev.,* **124,** 1865–1891.

Cammas, J.-P., and Coauthors, 1999: FASTEX IOP 17 cyclone: Introductory synoptic study with field data. *Quart. J. Roy. Meteor. Soc.,* **125,** 3393–3414.

Cardone, V. J., R. E. Jensen, D. T. Resio, V. R. Swail, and A. T. Cox, 1996: Evaluation of contemporary ocean wave models in rare extreme events: The "Halloween Storm" of October 1991 and the "Storm of the Century" of March 1993. *J. Atmos. Oceanic Technol.,* **13,** 198–230.

Chang, E. K. M., 1993: Downstream development of baroclinic waves as inferred from regression analysis. *J. Atmos. Sci.,* **50,** 2038–2053.

——, 1999: Characteristics of wave packets in storm tracks. Part II: Seasonal and hemispheric variations. *J. Atmos. Sci.,* **56,** 1729–1747.

——, 2000: Wave packets and life cycles of troughs in the upper-troposphere: Examples from the Southern Hemisphere summer season of 1984/85. *Mon. Wea. Rev.,* **128,** 25–50.

——, and D. B. Yu, 1999: Characteristics of wave packets in the upper troposphere. Part I: Northern Hemisphere winter. *J. Atmos. Sci.,* **56,** 1708–1728.

Davis, C. A., E. D. Grell, and M. A. Shapiro, 1996: The balanced dynamical nature of a rapidly intensifying oceanic cyclone. *Mon. Wea. Rev.,* **124,** 3–26.

Gibson, R., P. Kållberg, S. Uppala, A. Hernandez, A. Nomura, and E. Serrano, 1997: ERA description. Reanalysis Project Rep. Series, Vol. 1, ECMWF, 72 pp.

Gage, K. S., and G. C. Reid, 1986: The tropical tropopause and the El Niño of 1982–1983. *J. Geophys. Res.,* **91,** 13 315–13 317.

——, and ——, 1987: Longitudinal variations in tropical tropopause properties in relation to tropical convection and ENSO events. *J. Geophys. Res.,* **92,** 14 197–14 203.

Hakim, G. J., L. F. Bosart, and D. Keyser, 1995: The Ohio Valley wave-merger cyclogenesis event of 25–26 January 1978. Part I: Multiscale case study. *Mon. Wea. Rev.,* **123,** 2663–2692.

——, D. Keyser, and L. F. Bosart, 1996: The Ohio Valley wave-merger cyclogenesis event of 25–26 January 1978. Part II: Diagnosis using quasigeostrophic potential vorticity inversion. *Mon. Wea. Rev.,* **124,** 2176–2205.

Hartmann, D. L., and P. Zuercher, 1998: Response of baroclinic life cycles to barotropic shear. *J. Atmos. Sci.,* **55,** 297–313.

Highwood, E. J., and B. J. Hoskins, 1998: The tropical tropopause. *Quart. J. Roy. Meteor. Soc.,* **124,** 1579–1604.

Hoerling, M., K. Schaak, and A. Lenzen, 1991: Global objective tropopause analysis. *Mon. Wea. Rev.,* **119,** 1816–1831.

Hoinka, K. P., 1998: Statistics of the global tropopause pressure. *Mon. Wea. Rev.,* **126,** 3303–3325.

——, 1999: Temperature, humidity, and wind at the global tropopause. *Mon. Wea. Rev.,* **127,** 2248–2265.

Hoskins, B. J., 1991: Towards a PV–θ view of the general circulation. *Tellus,* **43AB,** 27–35.

——, and P. Berrisford, 1988: A potential vorticity perspective of the storm of 15–16 October '87. *Weather,* **43,** 122–129.

——, M. E. McIntyre, and A. W. Robertson, 1985: On the use and significance of isentropic potential vorticity maps. *Quart. J. Roy. Meteor. Soc.,* **111,** 877–946.

Hsu, C. J., and R. A. Plumb, 2000: Nonaxisymmetric thermally driven circulations and upper-tropospheric monsoon dynamics. *J. Atmos. Sci.,* **57,** 1255–1276.

Huo, Z., D.-L. Zhang, J. Gyakum, and A. Staniforth, 1995: A diagnostic analysis of the superstorm of March 1993. *Mon. Wea. Rev.,* **123,** 1740–1761.

Johnson, D. R., 1989: The forcing and maintenance of global monsoonal circulations: An isentropic analysis. *Advances in Geophysics,* Vol. 31, Academic Press, 43–316.

Juckes, M., 1994: Quasigeostrophic dynamics of the tropopause. *J. Atmos. Sci.,* **51,** 2756–2768.

Junger, S., 1997: *The Perfect Storm: A True Story of Men Against the Sea.* Norton, 227 pp.

Kalnay, E., and Coauthors, 1996: The NCEP/NCAR 40-Year Reanalysis Project. *Bull. Amer. Meteor Soc.,* **77,** 437–471.

Kanamitsu, M., 1989: Description of the NMC global data assimilation and forecast system. *Wea. Forecasting,* **4,** 334–342.

——, and Coauthors, 1991: Recent changes implemented into the global forecast system at NMC. *Wea. Forecasting,* **6,** 425–435.

Kocin, P. J., and L. W. Uccellini, 1990: *Snowstorms along the Northeastern Coast of the United States: 1995 to 1985.* Amer. Meteor. Soc., 280 pp.

——, P. N. Schumacher, R. F. Morales, and L. W. Uccellini, 1995: Overview of the 12–14 March 1993 Superstorm. *Bull. Amer. Meteor. Soc.,* **76,** 165–182.

Martin, J. E., 1998: The structure and evolution of a continental winter cyclone. Part I: Frontal structure and the occlusion process. *Mon. Wea. Rev.,* **126,** 303–328.

McIntyre, M., 1988: The dynamical significance of isentropic distributions of potential vorticity and low-level distributions of potential temperature. *Proc. The Nature and Prediction of Extratropical Weather Systems,* Vol. 1, Reading, United Kingdom, ECMWF, 237–259.

——, and W. A. Norton, 2000: Potential vorticity inversion on a hemisphere. *J. Atmos. Sci.,* **57,** 1214–1235.

Mo, K. C., X. L. Wang, R. Kistler, M. Kanamitsu, and E. Kalnay, 1995: Impact of satellite data on the CDAS–Reanalysis system. *Mon. Wea. Rev.,* **123,** 124–139.

Morgan, M. C., and J. W. Nielsen-Gammon, 1998: Using tropopause maps to diagnose midlatitude weather systems. *Mon. Wea. Rev.,* **126,** 2555–2579.

Nakamura, M., and R. A. Plumb, 1994: The effects of flow asymmetry on the direction of Rossby wave breaking. *J. Atmos. Sci.,* **51,** 2031–2045.

Namias, J., and P. F. Clapp, 1944: Studies of the motion and development of long waves in the westerlies. *J. Meteor.,* **1,** 57–77.

Newman, M., P. D. Sardeshmukh, and J. W. Bergman, 2000: An assessment of the NCEP, NASA, and ECMWF reanalyses over the tropical west Pacific warm pool. *Bull. Amer. Meteor. Soc.,* **81,** 41–48.

Nielsen-Gammon, J. W., 1995: Dynamical conceptual models of upper-level mobile trough formation: Comparison and application. *Tellus,* **47A,** 705–721.

——, and R. J. Lefevre, 1996: Piecewise tendency diagnosis of dynamical processes governing the development of an upper-tropospheric mobile trough. *J. Atmos. Sci.,* **53,** 3120–3142.

O'Connor, F. M., G. Vaughan, and H. De Backer, 1999: Observations of subtropical air in the European mid-latitude lower stratosphere. *Quart. J. Roy. Meteor. Soc.,* **125,** 2965–2986.

Orlanski, I., and J. Katzfey, 1991: The life cycle of a cyclone wave in the Southern Hemisphere. Part I: Eddy energy budget. *J. Atmos. Sci.,* **48,** 1972–1998.

Peters, D., and D. W. Waugh, 1996: Influence of barotropic shear on the poleward advection of upper-tropospheric air. *J. Atmos. Sci.,* **53,** 3013–3031.

Polvani, L. M., and R. A. Plumb, 1992: Rossby wave breaking, microbreaking, filamentation, and secondary vortex formation: The dynamics of a perturbed vortex. *J. Atmos. Sci.,* **49,** 462–476.

Postel, G. A., and M. H. Hitchman, 1999: A climatology of Rossby wave breaking along the subtropical tropopause. *J. Atmos. Sci.,* **56,** 359–373.

Randel, W. J., F. Wu, and D. J. Gaffen, 2000: Interannual variability of the tropical tropopause derived from radiosonde data and NCEP reanalyses. *J. Geophys. Res.,* **105,** 15 509–15 523.

Raymond, D. J., 1992: Nonlinear balance and potential-vorticity thinking at large Rossby number. *Quart. J. Roy. Meteor. Soc.,* **118,** 987–1015.

Reid, G. C., and K. S. Gage, 1981: On the annual variation in height of the tropical tropopause. *J. Atmos. Sci.,* **38,** 1928–1938.

——, and ——, 1996: The tropical tropopause over the western Pacific: Wave driving, convection, and the annual cycle. *J. Geophys. Res.,* **101,** 21 233–21 241.

Salmon, E. M., and P. J. Smith, 1980: A synoptic analysis of the 25–26 January 1978 blizzard cyclone in the central United States. *Bull. Amer. Meteor. Soc.,* **61,** 453–460.

Santer, B. D., J. J. Hnilo, T. M. L. Wigley, J. S. Boyle, C. Doutriaux, M. Fiorino, D. E. Parker, and K. E. Taylor, 1999: Uncertainties in observationally based estimates of temperature change in the free atmosphere. *J. Geophys. Res.,* **104,** 6305–6333.

Schubert, S. D., R. B. Rood, and J. Pfaendtner, 1993: An assimilated dataset for earth science applications. *Bull. Amer. Meteor. Soc.,* **74,** 2331–2342.

Shapiro, L. J., and J. L. Franklin, 1995: Potential vorticity in Hurricane Gloria. *Mon. Wea. Rev.,* **123,** 1465–1475.

Thorncroft, C. D., B. J. Hoskins, and M. E. McIntyre, 1993: Two paradigms of baroclinic life-cycle behaviour. *Quart. J. Roy. Meteor. Soc.,* **119,** 17–55.

Thorpe, A. J., 1986: Synoptic-scale disturbances with circular symmetry. *Mon. Wea. Rev.,* **114,** 1384–1389.

Tomas, R. A., and P. J. Webster, 1994: Horizontal and vertical structure of cross-equatorial wave propagation. *J. Atmos. Sci.,* **51,** 1417–1430.

Trenberth, K. E., 1991: Storm tracks in the Southern Hemisphere. *J. Atmos. Sci.,* **48,** 2159–2178.

Vaughan, G., and C. Timmis, 1998: Transport of near-tropopause air into the lower midlatitude stratosphere. *Quart. J. Roy. Meteor. Soc.,* **124,** 1559–1578.

Webster, P. J., and J. R. Holton, 1982: Cross-equatorial response to middle-latitude forcing in a zonally varying basic state. *J. Atmos. Sci.,* **39,** 722–733.